Soft Matter

PAPER

View Article Online
View Journal | View Issue

Cite this: *Soft Matter*, 2016, 12, 3888

Curvature-driven positioning of Turing patterns in phase-separating curved membranes†

Giulio Vandin,[a] Davide Marenduzzo,[b] Andrew B. Goryachev[c] and Enzo Orlandini*[a]

Received 9th February 2016,
Accepted 21st March 2016

DOI: 10.1039/c6sm00340k

www.rsc.org/softmatter

We introduce a new finite difference scheme to study the dynamics of Turing patterns of a two-species activator–inhibitor system embedded on a phase-separating curved membrane, modelling for instance a lipid bilayer. We show that the underlying binary fluid can strongly affect both the dynamical and the steady state properties of the ensuing Turing patterns. Furthermore, geometry plays a key role, as a large enough local membrane curvature can both arrest the coarsening of the lipid domains and position the patterns selectively at areas of high or small local curvature. The physical phenomena we observe are due to a minimal coupling, between the diffusivity of the Turing components and the local membrane composition. While our study is theoretical in nature, it can provide a framework within which to address intracellular pattern formation in systems of interacting membrane proteins.

1 Introduction

Domain and pattern formation on curved membranes are observed in a number of systems, ranging from condensed matter physics to cell biology.[1–11] Interesting examples relevant to the latter field are the formation of lipid rafts in eukaryotic cell membranes,[12] the spontaneous emergence of protein clusters when yeast cells polarise,[9,10] and the pattern formation, clustering and polar localisation of bacterial proteins.[13–16] In some cases at least, it is known that geometry is important, and pattern formation proceeds differently on a curved membrane with respect to a flat substrate; there is now indeed general consensus that curvature provides a cue to selectively recruit some peptides, or to reposition whole protein clusters.[17–20]

Here we consider a generic pattern forming system on a curved surface, where the patterning dynamics is coupled to an underlying phase separation. This nonequilibrium problem is broadly motivated by recent observations that protein localisation, in both bacteria and eukaryotes, is driven by interactions with the lipids in the interior cell membrane.[14–16,21] In particular, protein mobility has been shown to be affected by the local order or fluidity of a membrane:[21] similarly, interactions with different types of lipids can also profoundly affect protein dynamics.[22,23] It is therefore of interest to ask, more in general, how the lipid membrane dynamics can affect the pattern forming potential of a reaction–diffusion protein model, which is the topic of this work. The equations we propose are also theoretically intriguing because they probe the interplay between a close-to-equilibrium conserved dynamics (that of the phase-separating membrane) to a nonequilibrium system where the densities of chemical species need not be conserved (the Turing components). While we use the Turing system for simplicity, we note that Turing-like models can successfully describe, for example, the clustering of GTP-bound Cdc42 in budding yeast.[9,24,25]

We choose here to couple the Cahn–Hilliard and Turing dynamics in a minimal way, by postulating that the diffusivity of the activator and inhibitor which together create the Turing patterns may depend on the local composition of the (lipid) membrane; this is in line with the experimental evidence mentioned previously.[14–16,21] While in a system which reaches thermodynamic equilibrium a non-uniform diffusivity is immaterial for the long-time behaviour (as the statistics of the steady state is solely determined by the Boltzmann weight which is independent of the diffusion coefficient), this feature can instead have far-reaching effects in a nonequilibrium framework such as the one we consider here. As we shall see, curvature further enhances this potential. In particular, we show that on a flat geometry the coupling with lipid dynamics can both change the timescale and kinetic pathway en route to patterning, as well as the qualitative nature of the pattern ultimately formed (for instance from spots to stripes). On a curved surface, the Cahn–Hilliard coarsening may be arrested if the underlying free energy is curvature-dependent; this in turn can redirect the Turing pattern, for example to highly curved regions only.

From a more technical point of view, it is important to highlight that it is highly non-trivial to follow numerically the evolution of a system of partial differential equations with non-uniform

[a] *INFN, Dipartimento di Fisica, Università di Padova, via Marzolo 8, Padova, 35131 PD, Italy. E-mail: orlandini@pd.infn.it*
[b] *School of Physics and Astronomy, University of Edinburgh, Edinburgh EH9 3FD, UK*
[c] *Centre for Synthetic and Systems Biology, University of Edinburgh, Mayfield Road, Edinburgh EH9 3BF, UK*

† Electronic supplementary information (ESI) available. See DOI: 10.1039/c6sm00340k

diffusivity in curved space; as a result problems such as the one we discuss here cannot be addressed, for instance, within most finite element algorithms, such as the one we recently used to study constant-diffusion reaction–diffusion or phase separation models on generic surfaces.[26,27] This is because common algorithms exploit some symmetry properties of the standard Laplace–Beltrami operator, which are no longer present when the diffusion coefficient varies spatially. The alternative route we follow here is to develop a more versatile finite difference scheme, which can be generalised more easily than the finite element algorithms, at the price of a slightly inferior numerical accuracy.

This article is structured as follows. In Section 2 we review the basic components of our coupled model, namely the Cahn–Hilliard dynamics of phase separation and the Turing reaction–diffusion model on a flat surface; we also introduce the finite difference algorithm that was used to solve them. We further discuss the covariant equation with and without an explicit coupling of the dynamics with the local curvature of the membrane. In Section 3 we present the results of our simulations on differently shaped vesicles. Section 4 contains a brief discussion of our results and our conclusions.

2 Models and methods

The purpose of this paper is to study a system of coupled partial differential equations on curved (closed) manifolds. We chose to study the behaviour of such equations on a limited set of curved surfaces, to better exemplify the main features of the model. The general idea of our study is to show how the coupling between a phase-separating lipid membrane, obeying the Cahn–Hilliard dynamics, and a pattern-forming Turing system can induce the formation of structures only in localised regions of the system, and that these regions in a curved environment can be geometrically controlled.

2.1 Cahn–Hilliard dynamics for domain formation in a phase separating binary mixture

The phase separation in the membrane is modelled by the well studied Cahn–Hilliard equation,[28] describing a globally conserved system, the composition of the mixture, whose dynamics is governed by gradients in the chemical potential, a quantity which can be written as the functional derivative of the following free energy functional:

$$\mathcal{F}[\varphi] = \int d^2x \left[f(\varphi(\mathbf{x})) + \frac{\kappa}{2} |\nabla \varphi(\mathbf{x})|^2 \right],$$

where f is a Ginzburg–Landau-like function which displays a local maximum in the origin and two symmetric minima, which represent the two equilibrium phases of the field φ.

A physical picture of this model might be the following: in a system with two immiscible (*e.g.* lipid) phases A and B, the local concentration of the phase A being $\phi_A \in [0, 1]$ and the one of phase B defined as $\phi_B = 1 - \phi_A$, a single order parameter can be defined as their difference $\varphi = \phi_A - \phi_B = 2\phi_A - 1$, which contains all the information on the local composition, since the two fields are not independent. Thus, choosing a bulk free energy density of the form

$$f(\varphi) = \frac{1}{4}\varphi^4 - \frac{1}{2}\varphi^2$$

would induce an equilibrium configuration in which separate domains are formed with constant values $\varphi = 1$ corresponding to phase A and $\varphi = -1$ corresponding to phase B.

An extension of this simple model will be discussed in Section 2.3, where an additional term in the free energy is added, representing a linear coupling of φ with the local Gaussian curvature of the curved surface on which the field is defined.

2.2 Turing-like model for pattern formation

We now review the general Turing model, which we take as a prototypical example of pattern formation. The basic set-up is a nonlinear activator–inhibitor reactor–diffusion system, exemplified by the general set of equations (for simplicity we first review the standard, constant-diffusivity version):

$$\begin{cases} \dfrac{\partial u_1}{\partial t} = F(u_1, u_2) + D_1 \nabla^2 u_1 \\ \dfrac{\partial u_2}{\partial t} = G(u_1, u_2) + D_2 \nabla^2 u_2 \end{cases}.$$

General conditions for patterning require that: (i) a linearly stable equilibrium exists for the non-spatial problem (*i.e.* in the limit $D_1 = D_2 = 0$); and (ii) the same point in (u_1, u_2) space becomes an unstable equilibrium when the diffusive terms are included. This is the so-called diffusion-driven instability: to observe it it is crucial that the inhibitor diffusion coefficient D_2 needs to be bigger than a critical threshold, so that the inhibitor "escapes" from regions where higher concentrations of activator are present. This allows local growth in the activator concentration, and consequently the formation of patterns.

Among all possible systems forming Turing patterns, we focus her on the Gierer–Meinhardt model, with the rescaled set of equations

$$\begin{cases} \dfrac{\partial u_1}{\partial t} = \gamma\left(\dfrac{{u_1}^2}{u_2} - a u_2\right) + \nabla^2 u_1 \\ \dfrac{\partial u_2}{\partial t} = \gamma\left({u_1}^2 - u_2\right) + D\nabla^2 u_2 \end{cases},$$

where γ represents the spatial scale of the system and a is a free parameter.[29]

In this case, the conditions for the onset of a diffusion-driven instability are

$$0 < a < 1, \quad aD_2 > 3 + 2\sqrt{2}.$$

Therefore, when choosing $a = 0.5$, the critical D for the formation of patterns is $D_c = 6 + 4\sqrt{2}$; smaller values of D leave the uniform state stable. Note that the Gierer–Meinhardt model is here introduced as a simple generic model to describe patterns of finite sizes rather than macroscopic phase separation. A simple physical mechanism which would lead to such micro-phase separation is, for instance, when protein have both a

short-range attraction and a long-range repulsion, *e.g.*, due to electrostatics.[30] Another mechanism is *via* signalling: for instance, there are observations of stripey and wavy patterns formed by the small GTPase Rho protein in the plasma membrane.[31]

In our work, we consider a non-trivial extension of this model where the diffusion coefficient D is spatially varying, because it depends on the local composition of the underlying binary mixture φ. As we shall see, we find non-trivial patterns when D_c is between the values of the diffusion coefficients in the A-rich and B-rich phases. The functional dependence for the dependence of diffusivity on the local composition of the binary fluid is a sigmoidal one,

$$D(\varphi) = D_c + \frac{\Delta D}{2} + \frac{\Delta D}{1+\exp(-\nu(\varphi-\varphi_0))}. \quad (1)$$

where ΔD and ν are respectively the maximum deviation ΔD from D_c, and the sharpness ν of the transition. Furthermore, φ_0 represents a threshold value of the density-conserving field which is intermediate between that corresponding to an A-rich and a B-rich phase (in practice we chose $\varphi_0 = 0$). While our main emphasis is for spatially varying D through its dependence on φ, we will also compare the results when φ is substituted by the Gaussian curvature of the surface, $K(\mathbf{x})$.

2.3 Coupled model on curved surfaces

In the context of differential geometry, the definition of a system of partial differential equations (PDEs) on manifolds requires the choice of a consistent "covariantization" (*i.e.* the route through which Euclidean gradients become covariant derivatives). This is needed in order to write up a free energy functional appropriate for any curved geometry. The simplest way to do so (borrowed from general relativity) is to choose a minimal coupling. This is implemented by simply replacing the flat metric induced by the Euclidean scalar product with the Riemann metric g of the manifold. In other words, the following replacements are operated:

$$\eta_{\mu\nu} \to g_{\mu\nu}, \quad \partial_\mu \to D_\mu, \quad \nabla^2 \to {\nabla_{LB}}^2,$$

where $\eta_{\mu\nu} = \delta_{\mu\nu}$ is the euclidean metric represented by the 2×2 identity matrix, ∂_μ is the partial derivative along direction μ and D_μ the corresponding covariant derivative on the manifold, and ∇_{LB} is the Laplace–Beltrami operator on the manifold.

Consequently, the free energy of the compositional order parameter φ is rewritten as

$$\mathcal{F}[\varphi] = \int d^2u\sqrt{g}\left[\frac{1}{4}\varphi^4 - \frac{1}{2}\varphi^2 + \frac{\kappa}{2}g^{\mu\nu}(D_\mu\varphi)(D_\nu\varphi)\right],$$

which induces the following system of PDE:

$$\begin{cases} \dfrac{\partial\varphi}{\partial t} = {\nabla_{LB}}^2(\varphi^3 - \varphi - \kappa{\nabla_{LB}}^2\varphi) \\ \dfrac{\partial u_1}{\partial t} = \gamma\left(\dfrac{{u_1}^2}{u_2} - au_2\right) + {\nabla_{LB}}^2 u_1 \\ \dfrac{\partial u_2}{\partial t} = \gamma({u_1}^2 - u_2) + g^{\mu\nu}D_\mu(D(\varphi)D_\nu u_2) \end{cases}. \quad (2)$$

While the Cahn–Hilliard and Turing dynamics are only coupled through the diffusivity of the inhibitor, we consider two possible couplings to the curvature. On one hand, there is an intrinsic curvature effect on all equations of motion through the diffusive terms, which contain covariant, and geometry-dependent, derivatives. On the other hand, we also consider one case where the free energy contains an explicit coupling between local membrane composition, φ, and curvature. This term is motivated physically as certain lipids can be attracted by regions of high curvature.[11,19,20] To describe this phenomenon, we use the following modified free energy

$$\mathcal{F}[\varphi] = \int d^2u\sqrt{g}\left[\frac{1}{4}\varphi^4 - \frac{1}{2}\varphi^2 + \frac{\kappa}{2}g^{\mu\nu}(D_\mu\varphi)(D_\nu\varphi) + c\varphi K\right], \quad (3)$$

where c controls the strength of the coupling. Differently from previous works,[27] the field φ is coupled to the gaussian curvature, $K(\mathbf{u})$ of the surface. Simulations in which $K(\mathbf{u})$ is replaced by the mean curvature do not show significant differences in the overall dynamics of the system.

The equation for φ resulting from the new free energy is

$$\frac{\partial\varphi}{\partial t} = {\nabla_{LB}}^2(\varphi^3 - \varphi - \kappa{\nabla_{LB}}^2\varphi + cK). \quad (4)$$

It is useful to outline in some more detail some properties of the coupled model with direct coupling between φ and Gaussian curvature. First, recall that the classical Cahn–Hilliard equation ($c = 0$) involves the interplay of a bulk term $f(\varphi)$ and an interface term $\nabla^2\varphi$. The stationary equation reduces to a constant solution in the bulk of the single phases, equal to $\varphi = \pm 1$ (found by minimising the bulk term $f(\varphi)$), whereas in 1D the compositional profile close to an interface (placed at $x = 0$) can be found exactly to be $\varphi(x) = \tanh(x/\sqrt{2\kappa})$.

Now, consider the coupled system, so the case $c \neq 0$. The steady state, equilibrium solution of the Cahn–Hilliard equation is given by the solution of

$$\varphi^3(\mathbf{x}) - \varphi(\mathbf{x}) - \kappa\nabla^2\varphi(\mathbf{x}) + cK(\mathbf{x}) = 0.$$

Within the bulk part – where the laplacian term can be set to zero – we have a bifurcation diagram which reduces to only one equilibrium over a certain value of cK. Limiting ourselves to a region with constant curvature $\bar{K}$ for the sake of simplicity, the equilibria of the compositional order parameter are given by the equation $\varphi^3 - \varphi + c\bar{K} = 0$. In other words, the curvature acts as an external field which shifts the equilibria from $\varphi = \pm 1$ and favours one of them (for instance the negative one for $c\bar{K} > 0$). Furthermore, while for small values of $c\bar{K}$ both the $c = 0$ equilibria are metastable, above a critical value (at which one of the equilibria becomes an inflection point), there is a single solution, thereby effectively attracting only one of the two phases (A-rich or B-rich) to regions with curvature $\bar{K}$.

3 Results

We now follow the dynamics of the coupled (non-uniform Turing diffusivity) and uncoupled (constant Turing diffusivity)

systems, showing their apparent differences in the resulting dynamics and the equilibrium solutions.

3.1 Dynamics on a flat surface

To begin with, we consider the dynamics of the system on a flat surface. Numerical integration of eqn (2) has been performed on a triangular grid of $N = 8686$ points with periodic boundary conditions and by using the Adams–Bashforth–Moulton predictor–corrector method for the time evolution[32] with time step $\Delta t = 0.01$ (see Appendix A for more details on the algorithm).

Fig. 1 shows the time evolution of the φ field and of the activator field u_1: it is apparent that patterning occurs either in the A-rich phase regions ($\varphi = +1$) or very close to it: these are the regions where the value of $D(\varphi)$ is large enough to trigger a diffusion-driven instability in the Turing equations. More interestingly, by comparing the kinetics of the simple Turing system with the one coupled to the phase separation dynamics, one observes that the φ-dependent diffusivity leads to a different selection of pattern type (stripes *versus* spots) and of wavelengths. This can be quantified by computing the time evolution of the typical cluster size of the activator $L[u_1](t)$ as the first moment of the structure factor, see Fig. 2. In particular, for the Turing system (red, green and cyan curves) one observes an initial fast (exponential) growth, followed by a decay, due to the nonlinear component of the equation that stabilizes the Turing pattern, to the typical length of the resulting spatially modulated steady-state. Notice that in the coupled case the small time dynamic is characterised by very small fluctuations of $L[u_1]$. This is because the spatial configuration of the reactants becomes progressively homogeneous until the droplets of the pattern-allowing phase become large enough for the patterning to initiate. On the contrary, after this initial regime, the fluctuations become more important than in the uncoupled case. This is due to the heterogeneity of the domains size, to the shrinking of some patterns by Ostwald ripening and the change in shape of

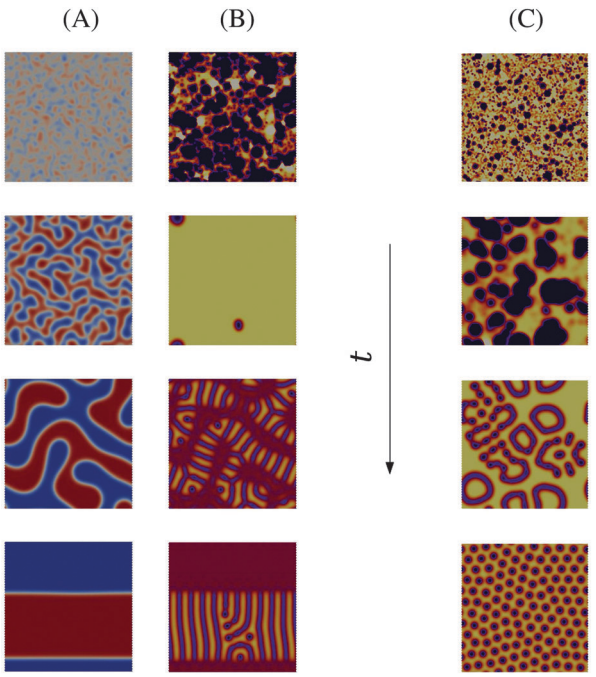

Fig. 1 Computed dynamics with periodic boundary conditions on a plane. (A) Snapshots of the Cahn–Hilliard phase separation dynamics for φ, starting from an initial random configuration. (B) Plots of the activator field u_1 in the Gierer–Meinhardt equations, with a diffusion coefficient coupled with φ. The uncoupled (constant diffusivity) dynamics of the activator is shown in sequence (C) for comparison. The parameter of the Cahn–Hilliard dynamics is $\kappa = 4$; the diffusivity function is characterised with a variation $\Delta D = 10$, and a sharpness $\nu = 10$. In all the figures the color scale of the patterning dynamics ranges from 0.1 (purple) to 4.5 (white) whereas the one referring to the coarsening dynamics ranges from $\varphi_- = -1$ (blue) to $\varphi_+ = +1$ (red).

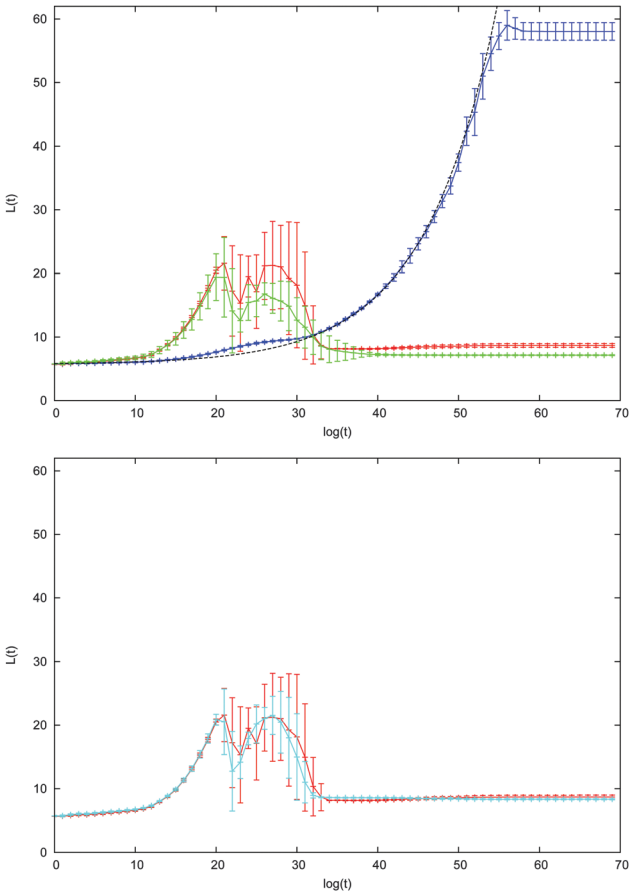

Fig. 2 Time evolution of the length scales of the interacting fields of Fig. 1. (top panel) The growing blue curve refers to the length scale of the binary mixture phases, $L[\varphi]$, undergoing the coarsening dynamics of Fig. 1A. Its behaviour is in agreement with the standard Cahn–Hilliard (model B) dynamics in finite domains. Indeed $L[\varphi]$ grows with time as $t^{1/3}$ (see dashed curve) until it reaches the system size. The red and green curves refer instead to the typical length scale of the Turing patterns, $L[u_1]$, evolving respectively with the coupled (Fig. 1B) and uncoupled (Fig. 1C) dynamics: the deviation of the two curves in the long time limit reflects the change between the striped (Fig. 1B) and the spotted (Fig. 1C) patterns. In the bottom panel we compare the time evolution of the Turing patterns length scale $L[u_1]$ in the coupled case when the Cahn–Hilliard coarsening is either comparable (red curve) or much faster (cyan curve) than the reaction–diffusion dynamics. In all cases the size of the bars (proportional to the fluctuations of $L[u_1]$) have been computed as the statistical error over 16 simulations.

the growing domains. The interplay between coarsening and patterning dynamics can be further explored by looking also at the extreme case in which the binary mixture coarsening is much faster then pattering (see bottom panel of Fig. 2). In particular we choose the extreme situation in which patterning occurs on a completely phase separated binary mixture. In this case (cyan curve) the fluctuations of $L[u_1]$ are less pronounced since the patterning dynamics occurs on an equilibrated (*i.e.* phase separated) substrate. In both coupled cases the stationary state value of $L[u_1]$ is higher than in the simple (*i.e.* uncoupled) Turing system indicating the selection of a stripey pattern rather than a more closely packed, spotted one. The fluctuations in the scale length of φ at steady state (blue curve) are caused by the fact that there are a few possible steady state configurations: either a circular domain of one phase within the other, or two parallel rectangular domains of the two different phases.

The difference between the coupled and uncoupled dynamics gives also rise to a distinct resolution of defects: while defects disappear altogether in the uncoupled model (Fig. 1C), defect annealing can be imperfect in the coupled version (Fig. 1B). This is because in the latter case defects may arise en-route to steady state due to coarsening, for example when two domains with different internal stripe orientation merge. In the case of Fig. 1B the boundaries of the pattern-allowing region are too far apart, so that the patterns are not constrained in a striped configuration in the whole domain, and the defects which are far enough from the boundaries are free not to cancel out. However, in a sufficiently small domain, the closeness of the boundaries forces the final configuration into the most symmetric one commensurate with the periodicity at the boundaries. In this case, if we choose a smaller domain for the simulation, evenly spaced stripes are formed at equilibrium (see Fig. S1, ESI†).

3.2 Dynamics on curved surfaces

We now turn to the results obtained from eqn (2) on a curved surface, beginning with an ellipsoidal geometry (either rod-like, prolate, or disc-like, or oblate). These simulations are more demanding in view of the anisotropic nature of the surface: we therefore used a less refined grid with $N = 2562$ points but with a much smaller integration time step $\Delta t = 0.001$. First, we focus on the case of intrinsic curvature, where the Gaussian curvature does not directly enter the bulk free energy. As in the flat case, patterns appear quickly in regions of high φ (Fig. 3).

We first neglect any explicit coupling of φ with the curvature of the surface. In this case the coarsening dynamics proceeds until phase separation is completed, irrespectively of the specific geometry of the surface, as already pointed out in previous works.[26,27] It is important to note that the only difference between Fig. 1(A and B) and Fig. 3 is the geometry of the surface. Remarkably, this is enough to select different patterns in steady state (spots in the curved geometry, stripes in the planar one). The kinetics we observe on the curved surface may also show multiple switches between patterns; for instance on a prolate ellipsoidal geometry the Turing reactants first form clusters; these then evolve transiently into stripes, and eventually into spots (see Fig. 3D).

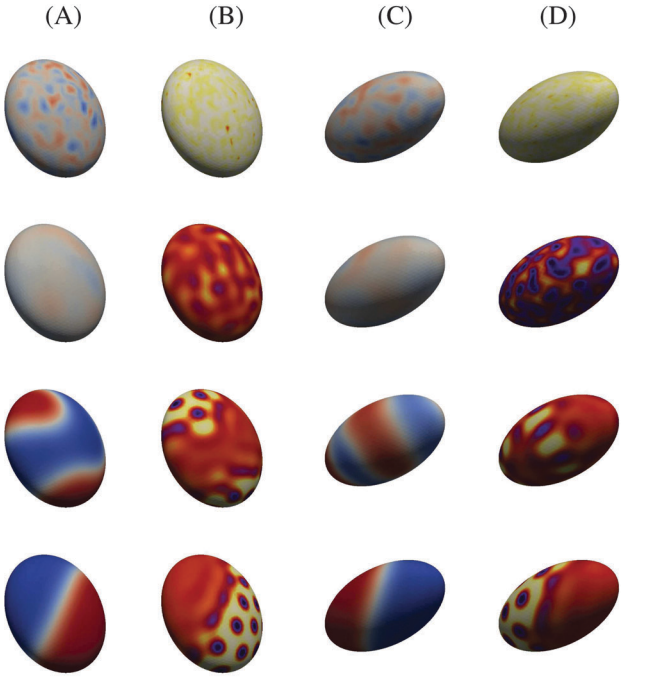

Fig. 3 Dynamics on an ellipsoidal geometry. (A) Displays the evolution of φ on an oblate ellipsoid, (B) is the corresponding u_1; (C) and (D) are analogous sequences for φ and u_1 respectively, on a prolate ellipsoid.

A second case of interest is that in which the curvature directly enters the free energy, so as to model differential targeting of lipids to areas of high curvature. This geometric coupling can arrest coarsening in the Cahn–Hilliard dynamics, so that the number of "lipid" domains is larger than one in steady state (see Fig. 4, 5 and Fig. S3, ESI†).[27] The number of domains in steady state depends on geometry: for instance we end up with two domains at the tip of a sufficiently prolate ellipsoid (see Fig. 4), whereas when modelling a sphere with Gaussian bumps, in steady state there may be as many domains as there are bumps (see Fig. 5A). A case with a single bump is reported in (Fig. 2A, ESI†).

To understand why the direct coupling between φ and curvature arrests the coarsening, we recall that as explained in Section 2.3 the curvature $K(\mathbf{x})$ may be viewed as an external field locally promoting high values of $|\varphi|$ (negative φ in the example of Fig. 4). If there are several places where $K(\mathbf{x})$ is high (*e.g.* a sphere with many bumps), then the coupling to the curvature favours the formation of a domain of φ in each of these locations. Because the overall composition of the binary mixture is conserved, and because the highly curved regions are fixed, it is not possible to join up these domains to form a single one without creating large interfaces which are thermodynamically unfavourable. The resolution of these competing factors is to arrest coarsening and end up with a multidomain steady state.[27] This argument also suggests that, according to the value of the surface tension and the coupling strength c to the curvature, the final number of domains can be controlled (see Fig. S1 and S3, ESI†).

Note that, while the Turing fields do not affect the dynamics of the binary system, the formation of Turing patterns depends

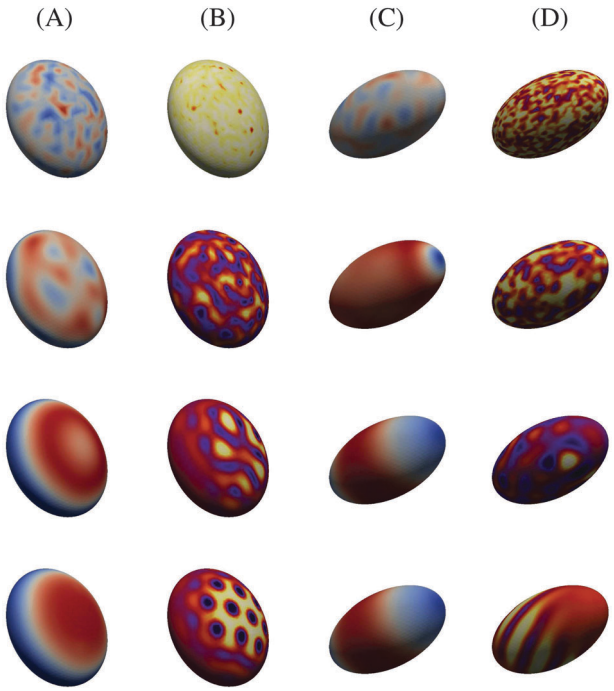

Fig. 4 Simulations with a direct coupling between curvature and φ in the free energy. In column (A) the evolution of the driving field φ on an oblate ellipsoid is shown, along with the corresponding patterns in the Turing species – localized in the zones with least curvature – on column (B). Columns (C) and (D) display the same for the case of a prolate ellipsoid. The size of the pattern-allowing domains is limited by the free-energy coupling, which, cannot be too high in order to keep the time variation of φ small enough for numerical stability.

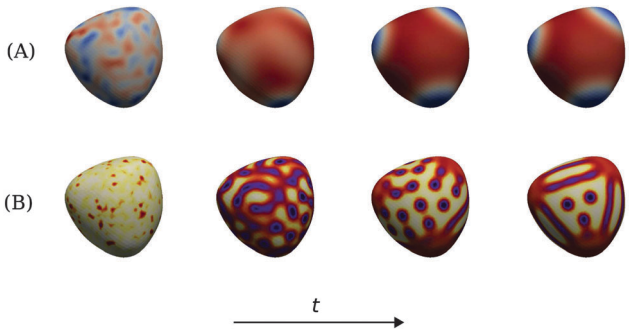

Fig. 5 Localized pattern formation on a sphere with four bumps. Similarly to other surfaces, the coupling promotes pattern formation on regions with smaller curvature. In row (A) the time evolution of φ is shown: the positive phase spreads throughout the central region of the surface, while the negative phase is allowed to be only on the bumps (higher-curvature regions). In row (B) the corresponding patterning of the activator field u_1 occurs in the lower-curvature regions which are rich in the $\varphi = 1$ phase. Note the coexistence of different patterns modes: striped around the bumps and spotted in the flat region.

strongly on the lipid concentration. In particular the coupling between the Turing dynamics and phase separation drives the patterns to domains with large values of φ, where the diffusivity of the inhibitor is large; as a result, in Fig. 4 and 5, patterns form in the low-curvature domains. Inverting the sign of the curvature coupling term c leads to the opposite behaviour with patterns now targeted to the high curvature regions, provided that the region with higher curvature is larger than the emerging lengthscale of the Turing patterns.

The pattern morphology (both over time and in steady state) is also determined geometrically, but in a subtler way. For instance, on an oblate ellipsoid local clusters of the activator create initially, to yield regular spot patterns at the flat sides (only the top one is shown in Fig. 4(A and B)). Instead, on a prolate geometry the initial dynamics is similar, but the pattern is later on relocated to a narrow central band on the ellipsoid, where it mutates to a set of tilted stripes. In this case, the selection of different patterns in steady state is simply related to the final symmetry of the domains which host them (an axially narrow symmetric band favours stripes in the perpendicular directions, two larger discs are isotropic and can accomodate spots).

In reality, the curvature of biological surfaces can vary more sharply than on the ellipsoids of Fig. 4; examples are budding cells such as yeast where a functional bump develops on the cell membrane. Situations like this can lead to a more complex dynamics in our coupled Cahn–Hilliard–Turing model. An example is shown in Fig. 5, where a sphere with four bumps is considered (see also Fig. S2A and B, ESI† for sphere with a single bump). The positive curvature at the bumps recruits negative domains of φ which stop coarsening and drive away the Turing patterns. As a result, stripes form which connect the negative φ bumps; this effectively creates four disconnected domains, each of which houses a regular array of activator spots (Fig. 5 and Movie S1, ESI†).

It is instructive to compare the patterns observed for the Turing dynamics coupled to the phase-separating boundary to a simpler version of the model where the diffusion coefficient of the Turing inhibitor depends directly on the surface curvature, and phase separation is not modelled. This can be done in practice by replacing φ with $K(\mathbf{x})$ in eqn (1). The results are shown in Fig. 6: while the patterns are now targeted to high or low curvature by hand, the dynamics by which they form is quite different. This is because the patterning domains are now static

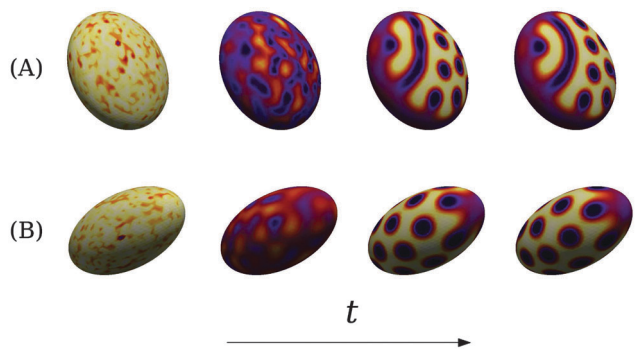

Fig. 6 Examples of Turing patterning dynamics when the inhibitor diffusivity depends on the (local) surface curvature, namely $D = D(K(\mathbf{x}))$. Rows (A) and (B) show the time evolution of the activator field u_1 respectively on an oblate and prolate ellipsoid. It can be seen that the resulting patterns differ from those obtained when the Turing system is coupled to the binary phase separation dynamics.

in space, whereas they are dynamic and linked to the Cahn–Hilliard kinetics in the coupled model. Consequently, we usually observe no switches in morphology over time, and as a result the steady states are different (compare Fig. 6 with Fig. 4 and Fig. S2B with Fig. S2C in the ESI†). In other words, the dynamic nature of the coupling between the Turing species and φ increases the pattern forming potential of the system.

4 Conclusions

In summary, in this work we have investigated by computer simulations the dynamics of a Turing pattern-forming system coupled to an underlying phase separation on a curved surface. This problem is motivated by recent experiments which suggest that some of the localised patterns formed by membrane-binding proteins in bacterial and eukaryotic cells are profoundly affected by their interaction with lipids on the membranes.[13–16,21] In our framework, therefore, the Turing model may be viewed as a minimal generic description of protein systems, and the Cahn–Hilliard equation may be seen as an approximate model of lipid dynamics. We note that the phase separation in cell membranes of living organisms does not proceed to completion but is arrested and results in the formation of nanoscale and mesoscale clusters;[33,34] the case we considered is simpler from a physical point of view, as it eventually results in macroscopic phase separation. This model is useful to see what generic effects the coupling of pattern formation to lipid dynamics can have. Furthermore, it should be possible to engineer *in vitro* a more similar situation to the one considered here, by studying pattern formation of proteins interacting with lipid bilayers or phase-separating vesicles.[35]

Our simulations show that on a flat geometry the dynamics of pattern formation through the Turing diffusion-driven instability is kinetically slowed down by the coarsening of lipid domains. The coarsening domains gradually increase the length scale at the disposal of the Turing reactants, and as a result these can create patterns which would otherwise be unstable in the absence of the phase separating background.

The situation is more intricate in a curved geometry.

There, lipids can be differentially attracted to regions with different local curvature, and this in turn drives the Turing pattern to either high or low curvature domains; the morphology of the patterns evolving dynamically and selected in steady state also subtly depend on the local geometry: for instance stripes form at narrow cylindrical bands, while spots are favoured on flatter regions. Surfaces with multiple bumps can feature spatial coexistence between different kinds of patterns.

It is important to highlight that these phenomena appear in the presence of a minimal coupling between Turing and lipid dynamics: all that we assumed was that the diffusivity of one of the Turing species (or equivalently the ratio between the diffusion coefficients of the two species) is non-uniform, but depends on the underlying lipid. This assumption is well grounded on recent observations that the motility of membrane-binding proteins depend on the local lipidic environment on the membrane,[21] hence it is more natural than other possible assumptions leading to qualitatively similar results, *e.g.* that the diffusivity of the pattern-forming species may itself directly be curvature-dependent.

On the one hand, we hope that our results will provide a useful if highly simplified framework within which to rationalise some of the aspects of pattern formation on biological membranes, or to stimulate studies on pattern formation on phase separating vesicles *in vitro*. On the other hand, the finite difference algorithm which we used can in principle also allow extension to cases in which polar or tensorial fields enter the dynamics. This is relevant, for instance, when the pattern forming species are elongated and can locally acquire orientational order, such as for rod-like proteins, or for protein fibrils.[36,37] These situations are still very rarely studied in non-Euclidean geometries, but our finite difference algorithm, which comes with an appropriate optimised discretisation of the curved surface (see Appendix A), could in principle address those.

Another possible extension of this study would be to replace the binary mixture model with mixtures with surfactant molecules. This would give rise to lipid phases with lamellar behaviour and probably different selection mechanism for the Turing patterns. Finally, although we focused exclusively on patterning and phase-separation dynamics on static surfaces it is reasonable to assume that a feedback mechanism between phase separating fields and shape changes in the membrane shape can be potentially important. Adding surface dynamics to our approach is beyond the scope of this study but is certainly an issue worth to be explored in the near future.

Appendix A: finite difference scheme on curved surfaces

Our algorithm is based on a finite-difference scheme already used in phase separation simulations.[38–40] The reason why we chose such an algorithm instead of the broadly used finite element methods – which are in general more precise – is that the latter are not suitable to treat scalar and tensor quantities, which can arise in the development of this kind of equations. The algorithms are based on a second order central finite difference scheme on an inhomogeneous grid, which slightly differs from usual central finite difference in that the forward and backward increments may not coincide:

- 1st derivative

$$\frac{\partial\varphi}{\partial x}(x,y) = \frac{1}{\Delta x_1\Delta x_2(\Delta x_1+\Delta x_2)}\left[\Delta x_2{}^2\varphi(x+\Delta x_1,y) + \left(\Delta x_1{}^2-\Delta x_2{}^2\right)\varphi(x,y) - \Delta x_1{}^2\varphi(x-\Delta x_2,y)\right] + o\left(\Delta x_i^2\right)$$

- 2nd derivative

$$\frac{\partial^2\varphi}{\partial x^2}(x,y) = \frac{1}{\Delta x_1\Delta x_2(\Delta x_1+\Delta x_2)}\left[\Delta x_2\varphi(x+\Delta x_1,y) - (\Delta x_1+\Delta x_2)\varphi(x,y) + \Delta x_1\varphi(x-\Delta x_2,y)\right] + o\left(\Delta x_i^2\right)$$

where we defined Δx_1 and Δx_2 respectively as the forward and backward increments along direction x, computed as the

lengths of the grid edges. We will now refer to the derivatives ∂_x, ∂_y as ∂_μ, with $\mu = 1, 2$ respectively.

The time evolution of a field f at vertex i is described by the spatially discretized equation

$$\dot{f}_\mathrm{i}(t) = F_\mathrm{i}(f, t)$$

where $F(f, t)$ is a function of f, and of time, differentiable at least once in t, which might contain nonlinear functions of f and the laplacian of f on the surface. The functions of f are simply discretized by replacing f with the value f_i at vertex i in the discrete form. A deeper discussion must be done for the Laplace–Beltrami operator – *i.e.* the covariant laplacian on the surface.

By using the expressions for the computation of the derivatives given above, it is possible to derive the values of the Riemann metric and the Levi-Civita connection on the surface as

$$g_{\mu\nu,\mathrm{i}} = \partial_\mu \vec{x}_\mathrm{i} \cdot \partial_\nu \vec{x}_\mathrm{i}, \quad \Gamma^\rho_{\mu\nu,\mathrm{i}} = g^{\rho\sigma} \partial_\sigma \vec{x}_\mathrm{i} \cdot \partial_\mu \partial_\nu \vec{x}_\mathrm{i},$$

with $\vec{x}_\mathrm{i}$ the coordinate vector of vertex i embedded in three-dimensional euclidean space, and $g^{\rho\sigma}_\mathrm{i}$ the inverse of the metric tensor. We choose as the directions μ, ν of derivation the edges connecting vertex i to two consecutive points among its nearest neighbours. Once these geometrical objects are computed for each point and each set of directions, we can write the full expression for the Laplace–Beltrami operator:

$$\Delta_{\mathrm{LB},\mathrm{i}} f_\mathrm{i} = g^{\mu\nu}_\mathrm{i} [\partial_\mu \partial_\nu f_\mathrm{i} - \Gamma^\sigma_{\mu\nu,\mathrm{i}} \partial_\sigma f_\mathrm{i}].$$

To ensure the isotropy of the operator, an average over the values of $F_\mathrm{i}(f, t)$ computed for every couple of contiguous directions (six or five values depending on the connectivity of the vertex) must be taken before integrating *via* the Adams–Bashforth–Moulton method.[32] This algorithm has been applied to a geodesic grid obtained from an icosahedron by means of a recursive dyadic triangulation scheme.[41] In order to compensate the consistently bigger error of this algorithm with respect to its finite elements counterpart, an optimization of the grid has been performed, treating the edges of the grid as springs with a rest length $l_0 = \pi R/100$ – where R is the radius of the sphere – as this choice minimizes the mismatches in the alignment of contiguous edges.[42] The outcome of this relaxation is a reduction of the errors by a factor five, which makes the algorithm much more reliable.

References

1 J. J. Amazon, S. L. Goh and G. W. Feigenson, *Phys. Rev. E: Stat., Nonlinear, Soft Matter Phys.*, 2013, **87**, 022708.
2 A. Veglio, A. Gamba, M. Nicodemi, F. Bussolino and G. Serini, *Phys. Rev. E: Stat., Nonlinear, Soft Matter Phys.*, 2009, **80**, 031919.
3 S. Semrau, T. Idema, L. Holtzer, T. Schmidt and C. Storm, *Phys. Rev. Lett.*, 2008, **100**, 088101.
4 J. Steinkühler, R. Lipowsky, P. Hildebrandt and R. Dimova, *Biophys. J.*, 2014, **106**, 278.
5 S. M. Loverde, V. Ortiz, R. D. Kamien, M. L. Klein and D. E. Discher, *Soft Matter*, 2010, **6**, 1419–1425.
6 W. M. Bement and G. von Dassow, *Curr. Opin. Cell Biol.*, 2013, **26**, 51–59.
7 V. D. Gordon, M. Deserno, C. M. J. Andrew, S. U. Egelhaaf and W. C. K. Poon, *Europhys. Lett.*, 2008, **84**, 48003.
8 T. Taniguchi, M. Yanagisawa and M. Imai, *J. Phys.: Condens. Matter*, 2011, **23**, 284103.
9 A. B. Goryachev and A. V. Pokhilko, *FEBS Lett.*, 2008, **52**, 1437–1443.
10 S. Okada, M. Leda, J. Hanna, N. Savage, E. Bi and A. Goryachev, *Dev. Cell*, 2013, **26**, 148–161.
11 P. Sens and M. S. Turner, *Phys. Rev. Lett.*, 2011, **106**, 238101.
12 G. van Meer, D. R. Voelker and G. W. Feigenson, *Nat. Rev. Mol. Cell Biol.*, 2008, **9**, 112–124.
13 P. A. Janmey and P. K. Kinnunen, *Trends Cell Biol.*, 2006, **16**, 538–546.
14 O. G. Mouritsen, *Cold Spring Harbor Perspect. Biol.*, 2011, **3**, a004622.
15 S. Alonso, U. Dietrich, C. Haendel, J. A. Kas and M. Bar, *Biophys. J.*, 2011, **100**, 939–947.
16 I. Barak and K. Muchova, *Int. J. Mol. Sci.*, 2013, **14**, 4050.
17 R. Lenarcic, *et al.*, *EMBO J.*, 2009, **28**, 2272–2282.
18 D. Bonazzi, A. Haupt, H. Tanimoto, D. Delacour, D. Salort and N. Minc, *Curr. Biol.*, 2015, **25**, 2677–2683.
19 B. J. Peter, H. M. Kent, I. G. Mills, Y. Vallis, P. J. G. Butler, P. R. Evans and H. T. Mcmahon, *Science*, 2003, **303**, 495–499.
20 N. S. Gov and A. Gopinathan, *Biophys. J.*, 2006, **90**, 454–469.
21 H. Strahl, F. Burmann and L. W. Hamoen, *Nat. Commun.*, 2014, **5**, 3442.
22 B. Alberts, *et al.*, *Molecular Biology of the Cell*, Garland Science, New York, 2002.
23 V. Y. Kiselev, D. Marenduzzo and A. B. Goryachev, *Biophys. J.*, 2011, **100**, 1261–1270.
24 E. Bi and H. O. Park, *Genetics*, 2012, **191**, 347–387.
25 A. S. Howell and D. J. Lew, *Genetics*, 2012, **190**, 51–77.
26 E. Orlandini, D. Marenduzzo and A. B. Goryachev, *Soft Matter*, 2013, **9**, 9311–9318.
27 D. Marenduzzo and E. Orlandini, *Soft Matter*, 2013, **9**, 1178–1187.
28 P. Chaikin and T. C. Lubensky, *Principles of Condensed Matter Physics*, Cambridge University Press, Cambridge, 2nd edn, 2000.
29 J. D. Murray, *Mathematical Biology II: Spatial Models and Biomedical Applications*, Springer, New York, 3rd edn, 2004.
30 F. Sciortino, S. Mossa, E. Zaccarelli and P. Tartaglia, *Phys. Rev. Lett.*, 2004, **93**, 055701.
31 W. M. Bement, M. Leda, A. M. Moe, A. M. Kita, M. E. Larson, A. E. Golding, C. Pfeuti, K. C. Su, A. L. Miller, A. B. Goryachev and G. von Dassow, *Nat. Cell Biol.*, 2015, **17**, 1471–1483.
32 J. H. Mathews and K. D. Fink, *Numerical Methods Using Matlab*, Prentice Hall, 4th edn, 2004.
33 K. Gowrishankar, S. Ghosh, S. Saha, C. Ruma, S. Mayor and M. Rao, *Cell*, 2012, **149**, 1353–1367.
34 A. Das, A. Polley and M. Rao, arXiv:1506.06928.

35 T. Baumgart, S. T. Hess and W. W. Webb, *Nature*, 2003, **425**, 821.
36 M. Simunovic, A. Srivastava and G. A. Voth, *Proc. Natl. Acad. Sci. U. S. A.*, 2013, **110**, 20396–20401.
37 K. Bohinc, A. Iglic and S. May, *Europhys. Lett.*, 2005, **71**, 145–151.
38 T. Taniguchi, *Phys. Rev. Lett.*, 1995, **76**, 4444.
39 P. Tang, F. Qiu, H. Zhang and Y. Yang, *Phys. Rev. E: Stat., Nonlinear, Soft Matter Phys.*, 2005, **72**, 016710.
40 J. F. Li, J. Fan, H. D. Zhang, F. Qiu, P. Tang and Y. L. Yang, *Eur. Phys. J. E: Soft Matter Biol. Phys.*, 2006, **20**, 449–457.
41 J. R. Baumgardner, *SIAM J. Numer. Anal.*, 1985, **22**, 1041.
42 H. Tomita, M. Satoh and K. Goto, *J. Comput. Phys.*, 2002, **183**, 307.

